Study of the time response of the ALICE TOF detector with muon pairs in ultraperipheral Pb-Pb collisions

Relatore: Presentata da:

Prof. Silvia Arcelli   Riccardo Galafassi

Correlatore:

Dott. Roberto Preghenella

Abstract

L'obiettivo del presente lavoro di tesi è quello di caratterizzare i dettagli della risposta temporale del rivelatore Time-of-Flight (TOF). Sono stati utilizzati eventi contenenti esclusivamente due muoni primari derivanti dal decadimento $J/\psi \rightarrow \mu^+\mu^-$, con J/ψ prodotte in collisioni ultra-periferiche tramite il processo di fotoproduzione esclusiva. Tali eventi costituiscono una condizione "pulita" per lo studio in oggetto, in quanto il basso numero di tracce presenti e la bassa probabilità di interazione dei muoni permettono di mantenere il fondo a livelli ottimali. Lo studio ha richiesto l'introduzione di una nuova variabile temporale $\Delta t_{\pm}$, sfruttando la correlazione tra il muone positivo e negativo, che permette l'eliminazione dell'incertezza su t_0, misura dell'istante in cui avviene l'urto.

La prima parte dell'analisi consiste nella selezione degli eventi associati al decadimento di J/ψ ultraperiferiche in muoni attraverso condizioni sulla massa invariante e la perdita di energia (dE/dx) nella (TPC). Quindi, poiché il modello puramente gaussiano non permette di effettuare un fit efficace del segnale $\Delta t_{\pm}$, un modello alternativo è stato utilizzato: il modello q-Gaussiano. Introducento infatti solo un grado di libertà si ottiene un notevole miglioramento nell'adattamento ai dati da cui è possibile ricavare i parametri caratteristici per la variabile $\Delta t_{\pm}$: $q = 1.54 \pm 0.06$ e $\sigma_{t_{TOF}} = 56.5 \pm 3.3$ ps. La risposta temporale del TOF può quindi essere caratterizzata utilizzando un modello composto, costituito da una Gaussiana per tempi inferiori al picco e da una q-Gaussiana per tempo maggiori. Questo modello è stato applicato a eventi ad alta molteplicità con parametri ottenuti tramite la deconvoluzione del segnale $\Delta t_{\pm}$ $q = 1.69 \pm 0.05$ e $\sigma = 57.4 \pm 3.2$ ps.

I dati utilizzati nella presente analisi sono stati raccolti durante l'autunno del 2015 in collisioni Pb-Pb a LHC con energia del centro di massa per coppia di nucleone di $\sqrt{s_{NN}} = 5.02$ TeV.

Contents

Chapter 1

The physics of ALICE

The 20th century is the triumph of quantum mechanics. Describing the laws that rule the microscopic word led to the formulation of a multitude of theories and discoveries. The scale of exploration beginning from the study of atoms and the theorization of the first atomic models, passing from the description of the nucleus, broke into the sub-atomic world and led to the formulation of the Standard Model which describes the elementary particles that form matter and the fundamental forces that interact between them.

1.1 The Standard Model

The Standard Model (SM) bases its roots on a theoretical formalism known as Quantum Field Theory (QFT). Within this framework fields are quantized and eventually endowed of mass, spin, and appropriated charges and constitute the base "ingredient" which constitutes the universe. Particles are just "quanta" of this field, bundles of energy, momentum and charges. There are four fundamental forces that operate between particles but just three have been incorporated within the Standard Model which are the strong, electromagnetic and weak forces, the last two unified in what is called electroweak force. Gravity is also an interaction, though it has not yet been included into the Standard Model because of its lacking of a renormalizable quantum field theory. Forces in QFT are a manifestation of the interaction with the field, mediated by "force carriers" or *bosons*. There are different types of bosons depending on the interaction: photons mediate the electromagnetic force, W^+, W^- and Z the weak interaction and eight *gluons* the strong one. The other type of particles described by the SM are *fermions*. These are the matter's constituents and they separate in two type: *quarks* and *leptons*. These can be classified into three "generations" of doublets which makes a total of 12 different particles to which there correspond an equivalent number of anti-particle. Quarks combine and form bound states obeying to quantum mechanics and they are found in nature in their most stable states, protons and neutrons, and in a assortment of excited

Three Generations of Matter (Fermions)

Figure 1.1: Summary of the particles described by the SM and their characteristic. We can note how the mass of quark and leptons is increasing as with the generation while charges remain invariant.

states. The Higgs boson has to be added to the picture to complete the description of the particles described by the Standard Model. It is the mass mediator which couples with W^+, W^- and Z, *leptons*, and *quarks* and it's responsible of giving mass to all elementary particles. In Figure 1.1 we can see a summary of all the particles of the SM. While not complete the Standard Model predictions have been verified by numerous experiments which contributed to its establishment in modern physics.

1.2 QCD

The strong force is described in the Standard Model through a theory called *Quantum Chromo Dynamics* (QCD). It is formulated assuming that for each quark's flavor there exist 3 *colour* charges (blue, green and red) and the corresponding anti-colour (anti-blue, anti-green and anti-red) for which they are invariant under transformation of the $SU(3)$ group (gauge theory). The strong field generated by these charges has as mediators 8

bosons called *gluons* which are carriers of colour charge.

Using empirical arguments it has been found impossible to find isolated quarks which are found only in combinations of colour neutral three quarks (*baryon*) or quark-antiquark (*meson*) particles. Those are direct consequences of what is called quark *confinement*. A more detailed study of the *coupling constant*[1] of the strong interaction α_S can give a more rigorous explanation for this phenomenon as well as what is called *asymptotic freedom*[1]. The dependency of α_S to the energy scale Q considered leads to two important limits:

$$\lim_{Q \to \infty} \alpha_S = 0,$$

$$\lim_{Q \to 0} \alpha_S = \infty.$$

The physical meaning of these two limits is that for high energy scales (small distances) α_S decreases to zero and quarks behave like free particles (*asymptotic freedom*). For low energy scales (large distances) quarks are confined in a limited region by the strong force with the consequences discussed above (quark *confinement*). Measurements of the dependence of α_S to the energy scale can be done through scattering experiments. As we can see in Figure 1.2 experimental data confirm the trend previously described.

1.3 Phase transition and QGP

The arguments introduced in the previous section are fundamental for the understanding of a particular state of the QCD: the Quark Gluon Plasma (QGP). Few instants after the Big Bang the temperature and density of the universe were extremely high and the energy was such that nuclei and atoms could not exist due to asymptotic freedom. Matter was in a state where quark and gluons were free, somehow similar to plasma, the Quark Gluon Plasma in fact. The fastly cooling and expanding universe led to a QCD phase transition from the QGP to ordinary matter where quarks can only exist in color-neutral particles called *hadrons* due to quark confinement.

To understand the physical behavior of QGP it is possible to use statistical mechanics. In this state free quark and gluons can be assimilated to a gas of free fermions and bosons which follow respectively Fermi-Dirac and Bose-Einstein statistics. Using this statistics it is possible to obtain the total energy density ϵ for a gas of fermions and bosons in natural units:

$$\epsilon = g_{tot} \frac{\pi^2}{30} T^4,$$

where $g_{tot} = g_b + 7/8 g_f$ and g_b and g_f are the degrees of freedom of the bosons and fermions particles. We can then obtain the pressure of the gas $P = \epsilon/3$. Considering

---

[1]When dealing with gauge theories a *coupling constant* is an adimensional number which determines the magnitude of the interaction of which it refers to. As in the case of strong force the constant can depend on the energy range considered.
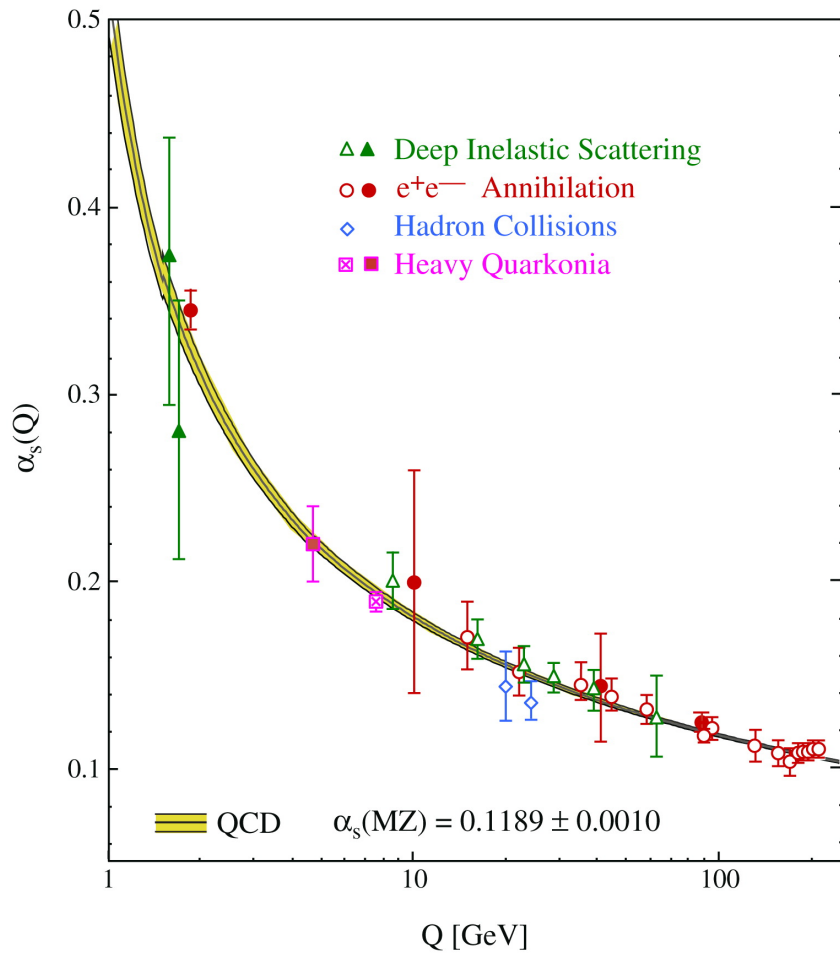
Figure 1.2: Measurements of the strong coupling constant α_S as a function of the energy scale Q in scattering experiments.

only two flavors of quark (up and down) we can calculate P for the initial (QGP) and final state (gas of pions). The pressure in the QGP state P_{QGP} will be:

$$P_{QGP} = \frac{37}{90}\pi^2 T^4.$$

When turning to the final state the result for the pressure of the pion gas P_π is not as immediate. In fact being $\alpha_S \sim 1$ it is not possible to treat QCD perturbatively. Lattice calculation are needed which lead to the formulation of the bag model [2]. On the computation of the pressure of the pion gas an additive constant B has to be incorporated in the equation leading to the pressure:

$$P_\pi = \frac{1}{30}\pi^2 T^4 + B.$$

Imposing the equality of the two pressures we can obtain the critical temperature

$$T_c = \left(\frac{45B}{17\pi^2}\right) \sim 170 \text{ MeV}.$$

As we can see in Figure 1.3 lattice QCD calculations are in agreement with the phase transition hypothesis. We can in fact observe a change of behavior and a rapid increase in the energy density when approaching the critical temperature T_c.

1.4   Experimental evidences towards QGP

The conditions for the QGP formation require extremely high temperature and energy density. It is possible to reproduce this condition in collisions of heavy ions in extremely powerful accelerators like the LHC. Within instants after the collision the QGP cools down and the free quarks and gluons hadronize. The direct study of the QGP is then possible only through the study of the products of the hadronization phase.

QGP probes are generally divided into two categories: *hard probes* which are evidences derived by the products of the first instants of the collision, in a pre-equilibrium phase of the QGP, characterized by high momentum partons; *soft probes* produced in the final stages of the collision characterized by lower momentum particles. An extensive list will not be carried through here but some of the most important are:

- EM probes

- jet quenching

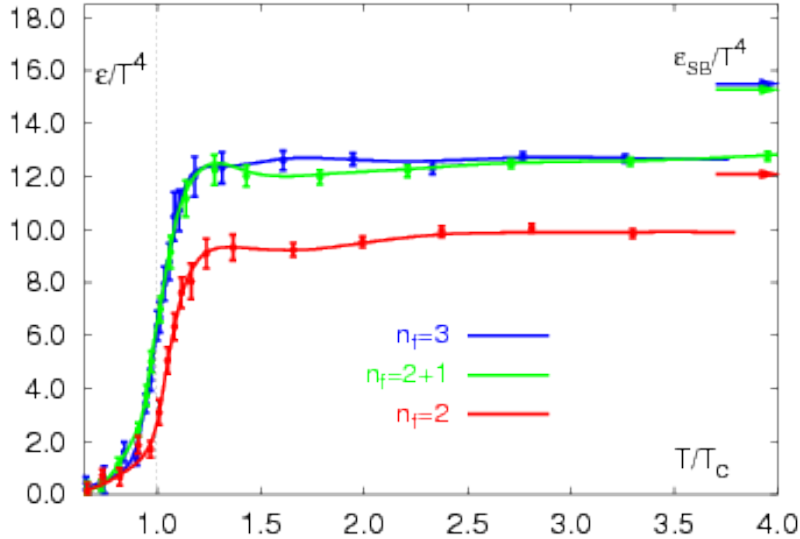- strangeness production

- J/ψ suppression

Figure 1.3: ϵ/T^4 as a function of the temperature in units of the critical temperature T_c for different number of flavors. The arrows indicate the limit for infinite temperatures for a gas of free quarks and gluons.

Electromagnetic probes

Strong electromagnetic radiation is emitted by the hot QGP from the very first instants following the collision. Real and virtual[2] photons are produced and, not feeling the strong force, they leave the thick medium without significant interaction. Because they are produced at a very early stage of the formation of the QGP they are referred as *direct photons* and they carry very important information about the characteristics of the QGP at its initial stage. Technical difficulties on their measurement though arise due to the weakness of the signal they produce in comparison to the background noise. *Background photons* are in fact produced in various processes which follow the formation of the QGP primarily due to scattering and decay of particles like π^0 and η. Even though studying direct photons could give important information about the QGP otherwise not obtainable, separating direct and background photons signals is not easily achieved experimentally.

---

[2]Virtual photons produced in the collision have limited lifetime. They annihilate and create a pair lepton-antilepton or dilepton which is then detected.
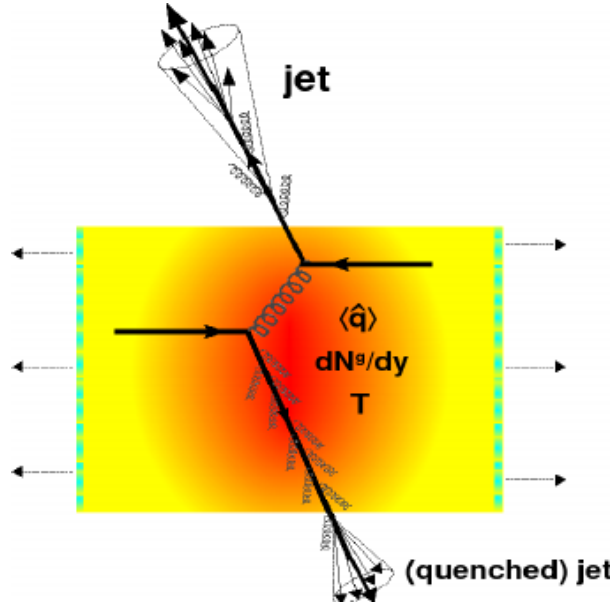
Figure 1.4: Schematic representation of jet quenching.

Jet quenching

During head-on nucleus-nucleus collisions elastic or inelastic scattering between partons[3] within the nucleus occurs. As a result of the collision two or more high transverse momentum partons ($p_t > 1$ GeV/c) may originate. This particles will then release their energy by successive emissions of other partons which then hadronize and result in a collimated *jet* of hadrons. When traversing the thick QGP particles lose energy at a higher rate in comparison to the motion in ordinary matter due to the strong interactions with the free partons. This results in lower energy jets when exiting the QGP. As it is evident from the schematic representation in Figure 1.4 the loss of energy will depend on the distance traveled by the parton in the QGP. The observation of lower energy jets or their disappearance is known as *jet quenching* and beside being a proof of the QGP formation it gives important information about the proprieties of the medium.

Strangeness enhancement

Strange quarks, unlike up and down are very rarely found in matter. They are unstable and quickly decay in the lighter, less massive states. Their production may occur in high energy collisions through processes that involve either the annihilation of gluons or quarks. While these processes are present even under the hypothesis of a dense gas of hadrons experimental results highlighted that the production of strange and anti-strange

---

[3]Collective name for the constituents of hadrons. Namely quarks and gluons.
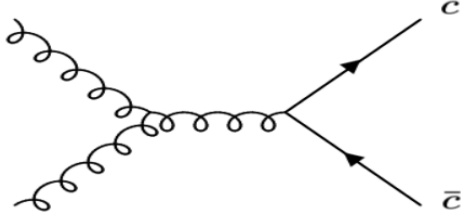
8

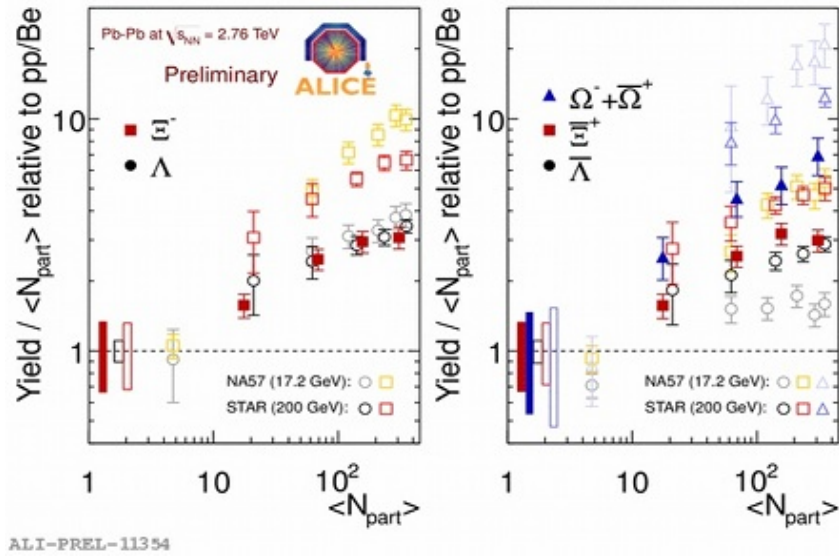Figure 1.5: Example of annihilation of gluons that produces a charm-anticharm pair.

Figure 1.6: Strangeness enhancement as a function of the number of partecipating nucleons N_{part}, measured at ALICE with Pb-Pb collision at $\sqrt{s_{NN}} = 2.76$ TeV [3]. We can observe how the relative number of Ξ, Ω and Λ baryons increases in comparison to those in pp and Be collisions. On the right the data are compared with SPS and RHIC.

quarks in resulting hadrons is excessive and not explainable under this framework. This phenomena, known as *Strangeness enhancement*, can be explained with the presence of the QGP. The dominant process for strange quark production is through annihilation of gluons in a process described by Feynman diagram of the type of that in Figure 1.5. The presence of free gluons in QGP makes this processes more likely to happen when compared to the quark gas model, explaining the enhancement.

The measurement of the *Strangeness enhancement* can be made counting the number of *strange* particles produced in a collision of heavy ions compared to p-p collisions. This increased production has been recorded in ALICE during the Pb-Pb data taking at $\sqrt{s_{NN}} = 2.76$ TeV revealed by the presence of high number of strange flavored baryons of the Ξ, Ω and Λ families. As we can see in Figure 1.6 the data follow the trend described.

J/ψ suppression

In high-energy collisions heavy mesons as Charmonia (bound state of $c\bar{c}$) and Bottomonia (bound state of $b\bar{b}$) are created. Predictions on their production rate led to the conclusion that a suppression of their yield is espected when QGP forms. The reason for this suppression can be found in a process called *color screening* [4]. At very high temperatures, as those that occur in the QGP, the large number of free color charges (gluons and quarks) interact with the heavy mesons modifying the bonding potential. In bound states like the J/ψ the bonding force becomes weaker due to the screening of the free charges, preventing the formation of the bound state. In comparison to p-p collisions a suppression of Charmonia and Bottomia yields is observed in nucleus-nucleus collisions.

Early calculation also predicted that the suppression would then be dependent on the temperature of the QGP increasing its effect for higher temperatures. Data taken at LHC in Pb-Pb collisions have shown instead a smaller suppression than that registered at SPS and RHIC in spite of the much higher temperatures reached [5]. A recombination mechanism of charm and anti-charm quarks is involved [6], where free $c\bar{c}$ pairs generated in incoherent interaction subsequent to the initial nucleus-nucleus collision, form bound states increasing the initial number of J/ψ produced. Being the strength of this effect dependent on the number of $c\bar{c}$ produced, increasing collision energies lead to higher J/ψ *regeneration* effect.

J/ψ suppression is quantified by an observable called nuclear modification factor R_{AA} which is defined as the ratio of J/ψ yields in Pb-Pb collisions to that in proton-proton collisions. In Figure 1.7 we can see the comparison between the data taken at LHC and RHIC. Both the suppression and regeneration effects are very evident. For the latter we can observe how for head on collisions (large $< N_{part} >$) the regeneration process becomes stronger.

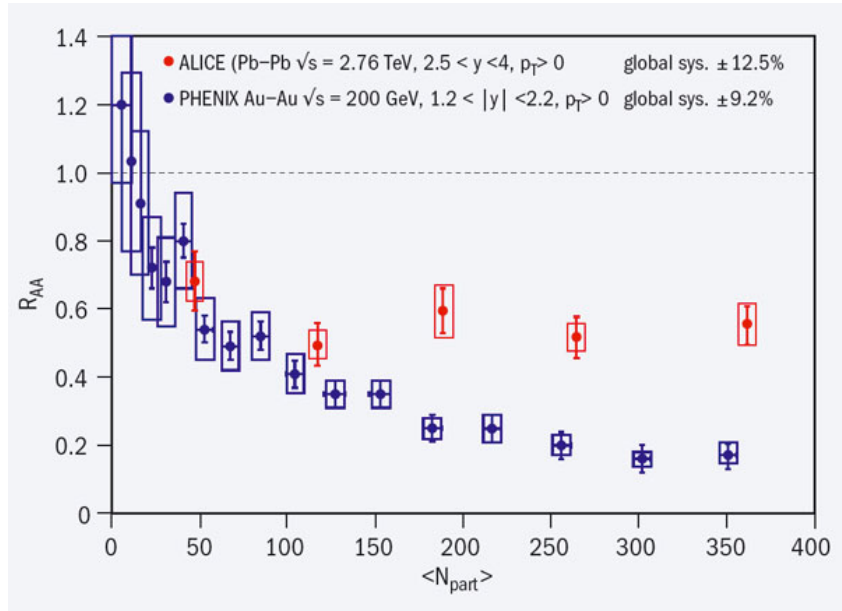Figure 1.7: The nuclear modification factor R_{AA} as a function of the number of nucleons $< N_{part} >$ involved.

Chapter 2

LHC, ALICE and the TOF detector

ALICE is one of the four main experiments on the LHC at CERN in Geneva. It has been designed to study strongly interacting matter at high temperature and energy density. In particular, in collision of heavy ions, it studies the formation and proprieties of the QGP. To carry out this task ALICE works in condition of very high multiplicity of tracks and a wide range of momentum.

In this chapter a brief introduction of the LHC will be given which will be followed by a more thorough description of the structure and functioning of ALICE and the TOF detector.

2.1 LHC

The Large Hadron Collider (LHC) is the largest and most powerful particle accelerator in the world. Sited on the border between Switzerland and France at more then 100 m below the ground it was able to reach the record energy for individual nucleus of 6.5 TeV. It lies in a 27 km long circular tunnel and it is composed of two rings in which beams of particles travel parallel in opposite direction at a speed approaching that of light. The circular motion is maintained using dipole magnets while quadrupole magnets are used to collimate the beam. A very strong magnetic field (up to 7.7 T) is necessary to maintain the particle's motion when reaching the desired energy. Superconductive magnets are used which operate at a temperature of ~ 1.9 K cooled using superfluid helium.

The beams cross in four interaction points where collisions between particles happen. Around the collision points the four main experiments are sited: ALICE, CMS, ATLAS and LHCb.

A schematic representation of LHC and the CERN accelerator complex is shown in Figure 2.1.

Figure 2.1: Schematic representation of the CERN accelerator complex. The biggest ring represent the LHC on which the main four experiments are sited.

2.2 ALICE

ALICE (A Large Ion Collider Experiment) focuses on the study of collisions of lead ions to understand how matters behaves when subjected to high energy density and strong interaction in the QGP state. Lighter ions collisions (including proton-proton collisions) are also studied at ALICE as they provide reference data for the heavy ion collision programs.

The design of ALICE consists of a central barrel part, devoted to track particles and identify them, constituted of various specific detectors which cover a polar angle between 45° and 135° and a forward region which extends outside the barrel in the beam direction. In the central barrel detectors are embedded in a large solenoid magnet with a nominal magnetic field of 0.5 T reused from the L3 experiment at LEP. In Figure 2.2 we can see a schematic representation of ALICE and its detectors which can be sorted based on their functions in:

- Specific detectors for *particle tracking* are included in the central barrel part, which can measure accurately momentum, position and loss of energy of particles in condition of very high multiplicity. Those are the Inner Tracking System (ITS), Time-Projection Chamber (TPC) and Transition Radiation Detector (TRD).

- The design of ALICE requires *particle identification* (PID) dedicated detectors to complement the tracking detectors. The Time Of Flight (TOF) and the High Momentum Particle Identification (HMPID) detectors, the former measuring the time of flight of particles the latter by measuring the presence and characteristics of Cherenkov Radiation, allow the identification of particles in a wide momentum range.

- *Calorimeters* are used to measure particle's energy. Most particles entering the calorimeter may in fact result in initiating a particle shower whose energy deposit can be measured by the calorimeter. The calorimeters included in ALICE are the following:

  - Photon spectrometer(PHOS),
  - Electro-Magnetic Calorimeter (EMCal);

- A *Muon spectrometer*

- *Forward and trigger* detectors which includes a series of detectors specialized in triggering and in the measurement of global event characteristics:

  - Forward Multiplicity Detector (FMD),
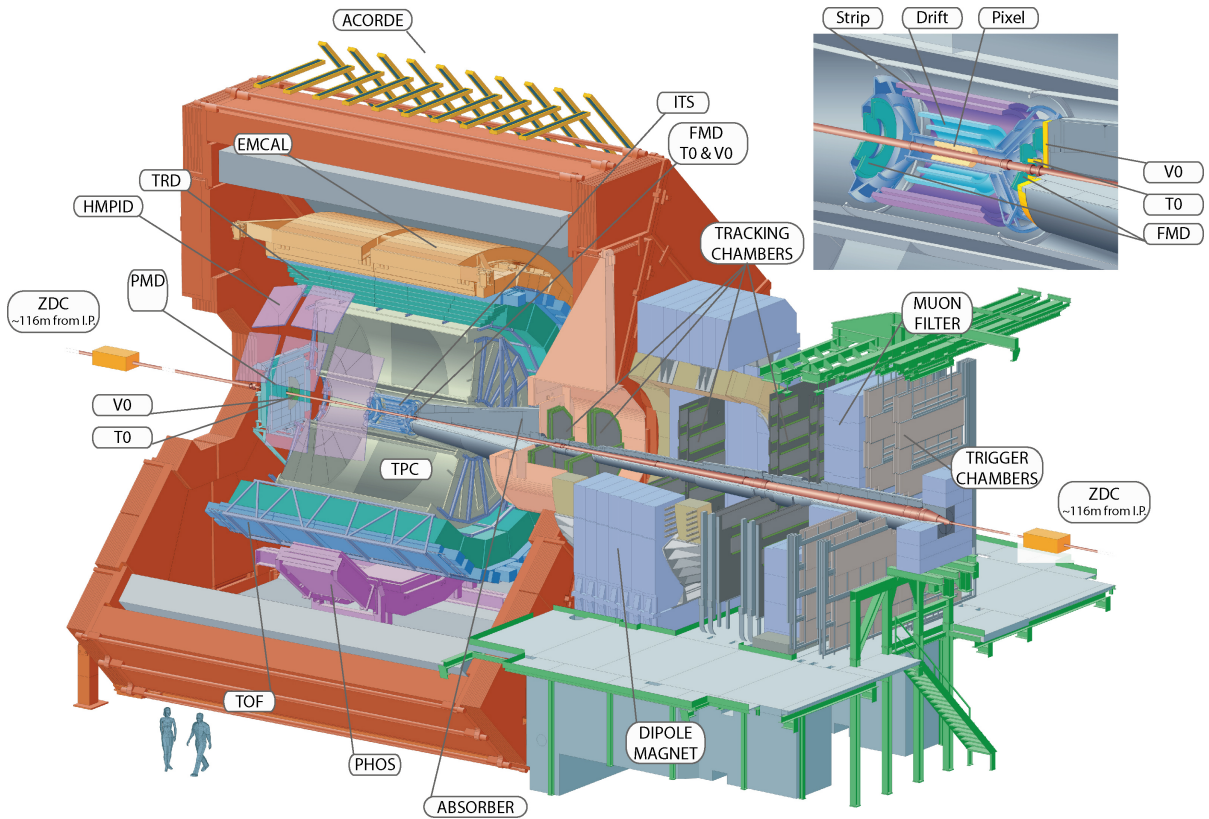 - Photon Multiplicity Detector (PMD),

Figure 2.2: ALICE schematic representation.

- Zero Degree Calorimeter (ZDC),

- V0 detector,

- T0 detector;

• The *ALICE Cosmic Ray Detector* (ACORDE) used for the study of cosmic rays.

In what follows we will proceed giving some more thorough description of some of the detectors just introduced. A more complete description of the TOF detector will be carried out in Section 2.3.

ITS

The ITS is the closest detector to the interaction point surrounding the beam pipe coaxially. Its main tasks are to measure the position of the primary vertex with a resolution of ~ 100 μm and the secondary vertex for decays of mesons as the B and D mesons, to track low momentum particles ($p < 200$ MeV/c) and to improve the reconstruction of particle tracks made by the TPC.

It consists of six concentric cylindrical layers of silicon detectors with inner radius of 4 cm, outer radius of 43 cm and it covers a rapidity range of $|\eta| < 0.9$. The dimensions of the ITS have been optimized in order to match perfectly with the TPC reconstructed tracks and to get the closest to the interaction point permissible by structure's limitations. Silicon Pixel Detectors (SPD) have been chosen for the innermost layers where high particle density is expected. For the outer layers, where the track density diminish, Silicon Drift Detectors (SDD) and double-sided Silicon micro-Strip Detectors (SSD) have been chosen. The analog readout of the outer layers allows for the measurement of dE/dx and it is therefore used for particle identification of low momentum particles.

TPC

The Time-Projection Chamber (TPC) constitutes the main tracking system of ALICE optimized for working in condition of extremely high multiplicity events as those in Pb-Pb collisions.

Cylindrical in shape it is inserted coaxially to the beam pipe in the central barrel and provides measurement of position, momentum and energy loss of charged particles. Its radius ranges from about 85 cm to about 250 cm and the length on the beam direction is about 500 cm. It covers a pseudo-rapidity region of $|\eta| < 0.9$ for full-length tracks and up to about $|\eta| = 1.5$ for partial tracks and an extensive p_t range from about 0.1 GeV/c to about 100 GeV/c.

The detector is made of a large cylindrical field cage filled with a mixture of gas which is ionized by charged particles traversing it. The ionisation electrons then drift towards the end plates for a distance up to 2.5 m on each side.

TRD

The Transition Radiation Detector main task is to provide electron (and positron) identification in the central barrel for momenta above 1 GeV/c, below which electrons can be identified using dE/dx in the TPC. The identification is made measuring the transition radiation emitted when an electron with momentum above 1 GeV/c crosses many layers of thin materials (a radiator). The TRD is designed to study in conjunction with the ITS and TPC the production of light and heavy vector-meson resonances.

The TRD radius ranges from 2.90 m to 3.68 m and covers a pseudo-rapidity of $|\eta| < 0.84$. It consists of 540 individual readout detector modules arranged in 18 super modules.

HMPID

The High-Momentum Particle Identification Detector main task is to improve the identification of high p_t hadrons beyond the interval in which identification is possible through

dE/dx and the TOF measurements. It is optimized for the discrimination between pions and kaons up to 3 GeV/c and kaons and protons up to 5 GeV/c.

It uses Ring Imaging Cherenkov (RICH) counters arranged in seven modules of 1.5×1.5 m^2 mounted in an independent support cradle. The radiator is a 15 mm thick layer of C_6F_{16} (perfluorohexane) liquid. Cherenkov photons are emitted when fast charged particles traverse the radiator and they get detected by a photon counter.

PHOS

The PHOton Spectrometer is a high-resolution electromagnetic spectrometer which covers a portion of the central barrel of pseudo-rapidity $|\eta| < 0.84$ and azimuthal angle $220° < \phi < 320°$. It is designed to study the thermal and dynamical properties of the initial phase of the collision by measuring low p_t direct photons and the jet quenching. To provide the high-energy resolution and granularity a high segmented electromagnetic calorimeter is paired to a Charged-Particle Veto (CPV) detector into what is called PHOS module. Each PHOS module is composed of 3584 detection cells of lead-tungstate ($PbWO_4$) scintillators.

Muon Spectrometer

The Forward Muon Spectrometer is a muon detector sited in the forward region outside the central barrel part covering a pseudo-rapidity region of $-4.0 < \eta < -2.5$. It is designed to study the production of heavy quark resonances as $J/\psi, \psi', \Upsilon, \Upsilon', \Upsilon''$ with high mass resolution through the $\mu^+\mu^-$ decay channel.

The spectrometer consists of the following components:

- a passive front absorber to absorb hadrons and photons from the interaction vertex;

- a high-granularity tracking system of 10 detection planes;

- a large dipole magnet;

- a passive muon-filter wall, followed by four planes of trigger chambers;

- an inner beam shield to protect the chambers from primary and secondary particles produced at large rapidities.

2.3 The Time of Flight Detector

The Time of Flight (TOF) is an ALICE detector designed for particle identification through the time of flight technique. It covers a pseudo-rapidity region of $|\eta| \lesssim 0.9$ and it can identify particles in the intermediate momentum range, up to 2.5 GeV/c for pions
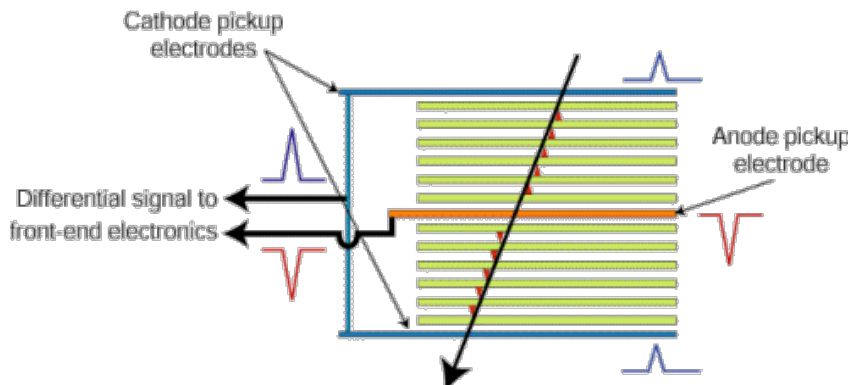
Figure 2.3: Schematic representation of a detail of the MRPC when a particle (black arrow) crosses it.

and kaons, 4 GeV/c for kaons and protons, with a π/K and K/p separation better than 3σ. Identification of large samples of particles in the mid-momentum region (up to about 1 GeV/c) is provided when the TOF is combined with dE/dx measurement in the ITS and TPC. This is essential for the physics of interest at ALICE in particular for the study of open heavy-flavored states and vector-meson resonances.

The TOF has been designed for large-coverage and efficient operativity using more that 10^5 independent channels in order to work at the highest predicted charged particle density of $dN/d\eta = 8000$.

2.3.1 Structure of the TOF

The TOF detector is cylindrical in shape, divided in 18 sectors or *supermodules* on the azimuthal angle and placed at a distance of ~ 4 m from the beam. In order to fulfill to the requirements of high particle density, high efficiency and resolution the technology chosen for the TOF detector is the Multi-gap Resistive-Plate Chamber (MRPC). A MRPC is an improvement of the RPC technology. The latter is based on the use of two parallel plates at which is applied a strong potential. A ionizable gas fills the area included between the plates. A particle with sufficient energy traveling through the gas can ionize it creating a electron-ion pair. The strong electric field created by the potential difference between the plates accelerates the pair. The two newly created charge particles in their motion may as well ionize the gas creating a new pair in a process which result in an avalanche effect. With the MRPC technology resistive plates are placed parallel to the electrodes in the gas at equivalent distances. The main advantage of this improvement is in the fact that individual avalanches are created in the gaps resulting in a final signal given by the sum of the single avalanches. In Figure 2.3 a schematic representation of a charged particle crossing the TOF shows the process just described.

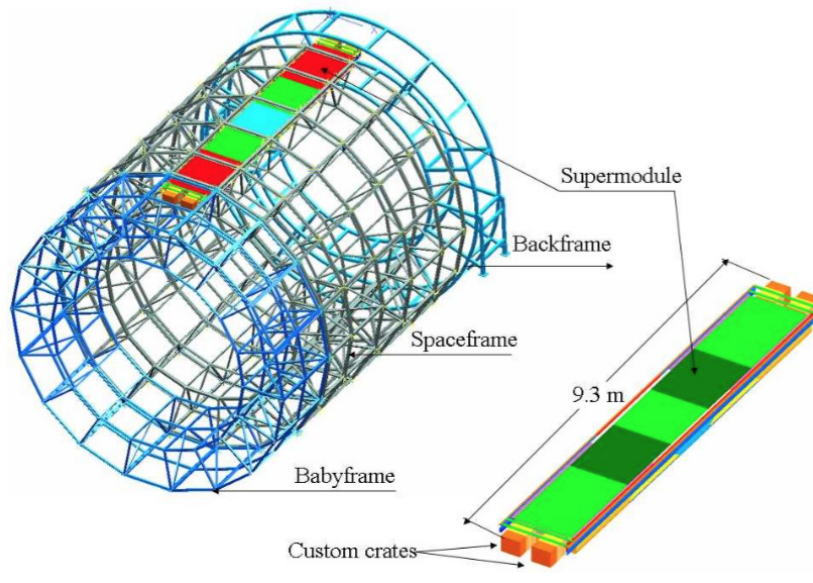Also, other advantages of the use of MRPC are:

Figure 2.4: Representation of one of the 18 supermodules and its positioning on the TOF frame.

- possibility of operating with the gas chamber at atmospheric pressure;

- the signal results in a peak well separated from zero and exponential tails are not present;

- high-gain operations are possible because the resistive plates quench the streamers so there are no sparks;

- generally easy construction techniques with commercially available materials.

Each supermodule is formed of five modules 128 cm wide of three different types differing for length and number of MRPC strips. The three types of modules are:

- two external modules, 1.78 m long with 19 MRPC strips;

- two intermediate modules, 1.37 m long with 19 MRPC strips;

- a central module, 1.17 m long with 15 MRPC strips.

We can see a representation of a supermodule in Figure 2.4. The disposition of the strips in the modules is designed to minimize the dead regions. To do so, adjacent strips slightly overlap on their edges.
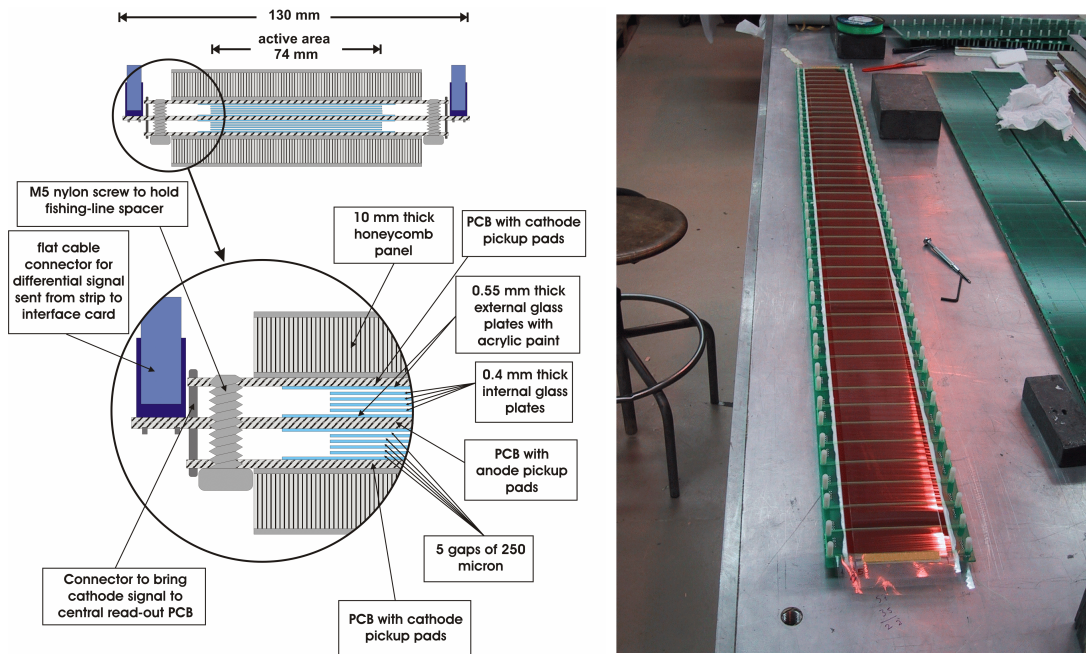
Figure 2.5: Section and detail of a MRPC strip (left) and full image of an assembled strip (right).

2.4 MRPC strips

The TOF units are composed of a 10-gap double-stack MRPC strip whith an active area of 7.4×120 cm² subdivided in 96 pads. Two external honeycomb aluminum plates placed on the external surfaces give support to the strip. Two stacks of five 0.4 mm thick glass plates are use as insulators to create the five 250 μm gaps between the two external plates (0.55 mm thick) which are coated with a resistive acrylic material. Two external PCBs (printed circuit boards) with cathode pickup and one internal PCB with anode pickup, placed between the stacks, contain the 96 pickup pads used to register the avalanche signal. Images of the strips can be seen in Figure 2.5. The whole strip is included in an airtight box where a gas mixture of $C_2H_2F_4$ (90%) $i - C_4H_{10}$ (5%) and SF_6 (5%) is injected to occupy a volume of 17.5 m³.

2.5 The TOF technique

The *time of flight* technique allows the identification of particles through the calculation of their mass using kinematic variables. Assuming the length of the trajectory L traveled by the particle to be know, the measurement of the time-of-flight t allows to calculate the velocity $v = L/t$. Due to the magnetic field in which the particle travels the momentum

of the particle is also easily obtainable by the measurement of the track's curvature. The mass of the particle m can then be extrapolated from the relativistic relation for the momentum $p = mv\gamma$ where γ is the Lorentz factor. The resulting formula for m express as a function of L, t and p is:

$$m^2 = \frac{p^2}{c^2}\left(\frac{c^2 t^2}{L^2} - 1\right)$$

Calculating the relative error $\frac{\delta m}{m}$ we obtain:

$$\frac{\delta m}{m} = \sqrt{\left(\frac{\delta p}{p}\right)^2 + \left(\frac{pt}{mL}\right)^4\left[\left(\frac{\delta t}{t}\right)^2 + \left(\frac{\delta L}{L}\right)^2\right]}$$

We note that dependence of $\frac{\delta m}{m}$ is quadratic on the momentum p. Considering two different particles of different mass m_1 and m_2 with the same momentum p and track length L we can define a quantity Δt for particle identification as the difference of time-of-flight between the two particles:

$$\Delta t = t_1 - t_2 = \frac{\gamma L}{p}\left(m_1 - m_2\right).$$

We can then quantify the capability of particle identification of the TOF in number of standard deviations n_σ using the equation:

$$n_\sigma = \frac{\Delta t}{\delta t}$$

The capability to separate different particles will then depends on the particle momentum as $n_\sigma \sim 1/p$. In Figure 2.6 we can see this dependence for different pairs of particles and for three different values of the time-of-flight resolution. Assuming an acceptance of $n_\sigma > 3\sigma$ we can note how electrons can be distinguished from pions only at low momentum ($p < 0.7$ GeV/c) while for kaons/pions and kaons/protons we find the values previously introduced of $\sim$2.5 GeV/c and $\sim$4 GeV/c respectively.
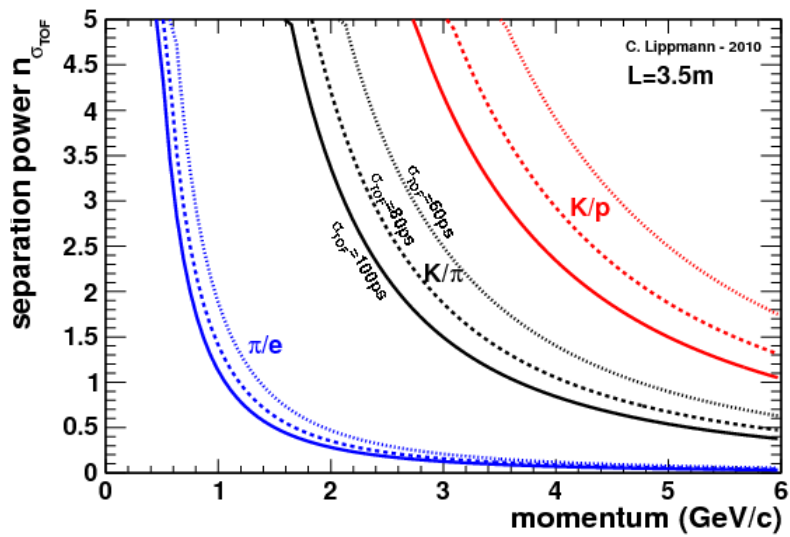
Figure 2.6: Graphs of n_σ as a function of the momentum for there different particles pairs. The curves are drawn for three estimated values of δt (σ_{TOF} on the graph).

Chapter 3

Analysis

The analysis has been performed using data taken during the fall of 2015 with Pb-Pb collisions at the centre-of-mass energy per nucleon pair of $\sqrt{s_{NN}} = 5.02$ TeV. From previous analyses of events with high moltiplicity it was observed that the TOF signal shape shows an evident non-gaussian tail on the right-hand side of it's maximum, as we can see in Figure 3.1. The analysis aims at studying the signal in low-molteplicity conditions, where low noise and a cleaner environment is expected to reveal the actual signal. This can help understanding whether the observed tails in the TOF signal are intrinsic characteristics of the apparatus or just an effect of particular particles. J/ψ mesons created in ultraperipheral collisions of lead ions are selected. In these processes a photon emitted from one of the ions interacts with the other ion and produce the meson according to the following reaction:

$$\gamma + Pb^+ \rightarrow J/\psi + Pb^+$$
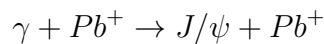
This meson has a relevant probability (the branching fraction is 5.961 ± 0.033 %[7]) of decaying in a pair of positive and negative muons,

$$J/\psi \rightarrow \mu^+ \mu^-$$
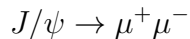
Muons are particulary useful because they leave a clear track in the TPC and reach the TOF detector with low interaction with the material and rare chance of decay. This type of event also allows us to use the correlation of the two tracks to reduce the width of the signal as we will see in the next section.

3.1 J/ψ - like events and particle detection.

Being the J/ψ mean life very short ($\sim 4 \times 10^{-21}$s) the decay happens very close to the interaction point. For this reason J/ψ-like events caracterized by the topology previously mentioned can be selected accepting only events with exactly one positive and one negative primary track.
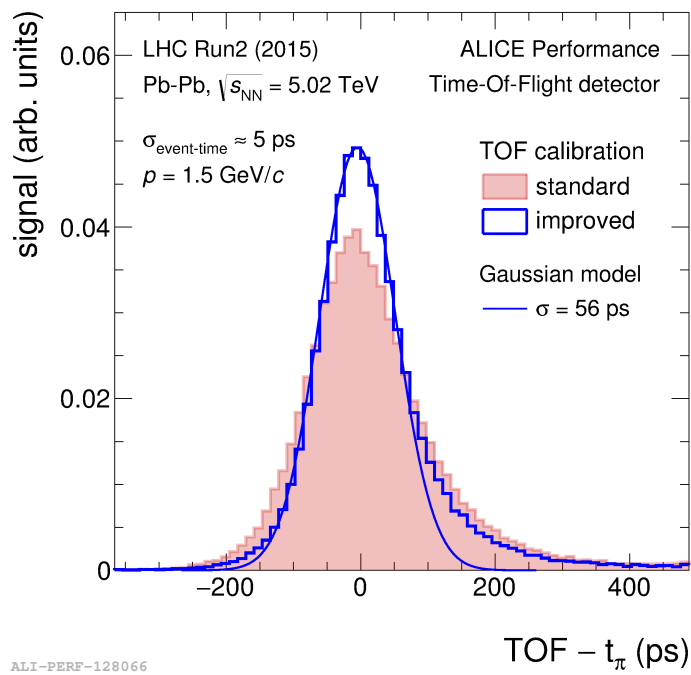
Figure 3.1: TOF signal, measured using pions in high molteplicity events of pions generated in nucleous-nucleous collisions. The data taking period is the same as the present analysis.
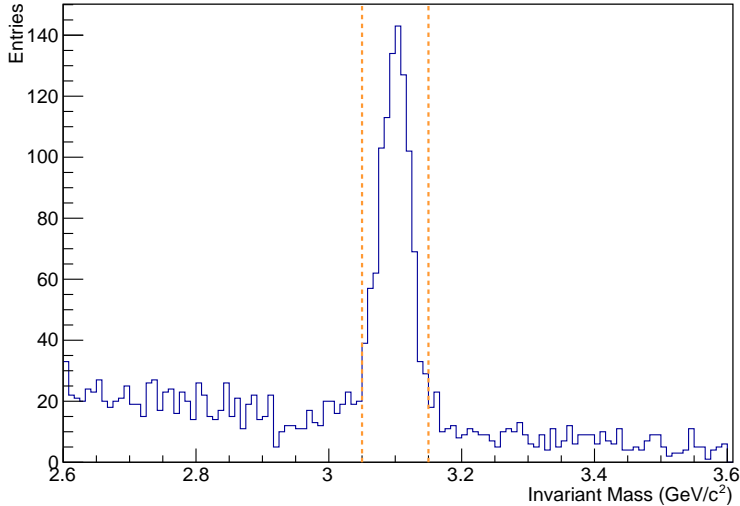
Figure 3.2: Invariant mass histogram. The orange vertical lines show where the mass cut have been applied.

A selection on the invariant mass of the reconstructed particle is then necessary to separate J/ψ leptonic decay from events with a similar topology (e.g. pions decay[1], Drell-Yan). The invariant mass $m_{J/\psi}$ of the J/ψ candidates can be reconstructed from the two tracks as:

$$m_{J/\psi} = \sqrt{(E^+ + E^-)^2 - (\mathbf{p}^+ + \mathbf{p}^-)^2},$$

where E and p are the particle's energy and momentum. The use of the apices $+$ and $-$, which will be carried on throughout the analysis, refer respectively to the positive and negative tracks. The choice of the upper and lower limits of application of the mass cut has been done trying to obtain the maximum signal/noise ratio without compromising excessively the statistic. In Figure 3.2 we can clearly see the peak of the J/ψ at the expected value ($m_{J/\psi} = 3096.900 \pm 0.006$ MeV [7]) and the values of 3.05 GeV/c^2 and 3.15 GeV/c^2 at which the noise component becomes relevant, and which correspond to a selection within a ± 2 standard deviations interval.

The loss of energy in the TPC has been used to discriminate amongst the possible J/ψ leptonic decays. J/ψ decay into an electron positron pair is infact also probable (the branching fraction is 5.971 ± 0.032 %[7]). As previously discussed muons interact

---

[1]Another possible form of decay of the J/ψ is into pions. That is a three-bodies decay $J/\psi \rightarrow \pi^+ \pi^0 \pi^-$, and the π^0, being neutral, is not detected in the TPC. When calculating the invariant mass of the J/ψ from the two charged tracks, it will result lower then the expected value due to the missing particle.
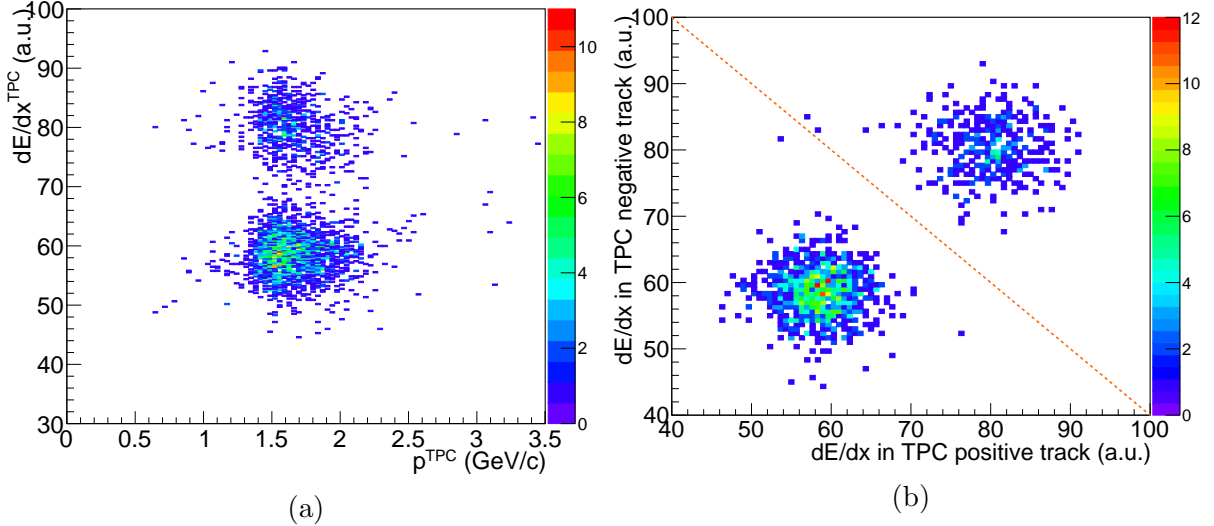
Figure 3.3: dE/dx for all J/ψ candidates in the mass range of 3.05 to 3.15 GeV/c^2 as a function of TPC's momentum (a). Negative track dE/dx as a function of that of the positive (b). Events below the orange dashed line corrispond to a sum of dE/dx of the two tracks less then 140 a.u. and are the muon candidates. Pions, having similar mass to muons, could also be present in this range.

less with the material of the detector and are therefore a cleaner probe then electrons. This is due to the fact that a reduced interacion with the material implies also a lower probability of mismatching the track to the TOF signal, expecially due to the lack of tracking history in the TRD. The specific energy loss dE/dx has caracteristic trends depending on the regime a particle is in. In the studied range of momentum, due to their mass difference (511 keV/c^2 for elctrons 105.7 MeV/c^2 for muons), electrons are ultrarelativistic and have a higher loss of energy compared to muons which are relativistic. From the correlation between the specific energy loss dE/dx and the momentum in the TPC, as we can see in Figure 3.3a, is possible to observe the separation between J/ψ decays into muon and electron pairs. To get a clearer separation between the two types of leptonic decay it is convenient to express the dE/dx of the positive track as a function of that of the negative as in Figure 3.3b.

The last cut for particle detection has been applied to the J/ψ transverse momentum. By selecting events where the J/ψ has transverse momentum lower than 0.1 GeV/c, the majority of J/ψ will be generated with a coherent photoproduction process [8]. The latter differs from incoherent photoproduction as the photon couples with the nucleus has a whole instead of interacting only with a single nucleon (incoherent). Muons generated from high transverse momentum J/ψ will get a boost with the possible result of having a large inbalance in the muon momenta, with one having large momentum and the other
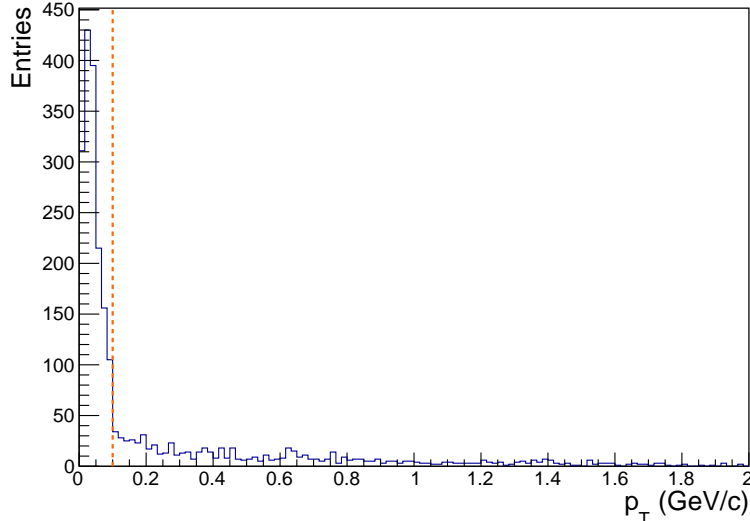
Figure 3.4: J/ψ transverse momentum. The cut has been applied at 0.1 GeV/c (orange line).

low momentum.

Previous studies [9] revealed an anomalous behavour of the 8th sector of TOF so it has been decided to remove the tracks hitting this sector from the present analysis.

3.2 Time signal and variables

As mentioned at the beginning of this chapter using the "two-tracks" J/ψ decay has advantages on reducing the signal width. To do so we can introduce the time variable Δt defined as:

$$\Delta t = t_{TOF} - t_{exp},$$

where t_{TOF} is the measurement of the particle time-of-flight with the TOF detector and t_{exp} is the time calculated integrating the momentum over the lenght of the track. We than have that, if t is the absolute time recorded by the TOF detector and t_0 is the absolute time at which the collision happens, we can express Δt as:

$$\Delta t = t - t_{exp} - t_0.$$

t_0 can be measured with high precision in high molteplicity events like those in Figure 3.1 (resolution $\sim$5 ps), while on an event with two tracks with a typical uncertanty of the order $\sim$200 ps. The TOF uncertanty is estimated at $\sim$60 ps and the variance will be

$$\sigma_{\Delta t}^2 = \sigma_t^2 + \sigma_{t_{exp}}^2 + \sigma_{t_0}^2$$
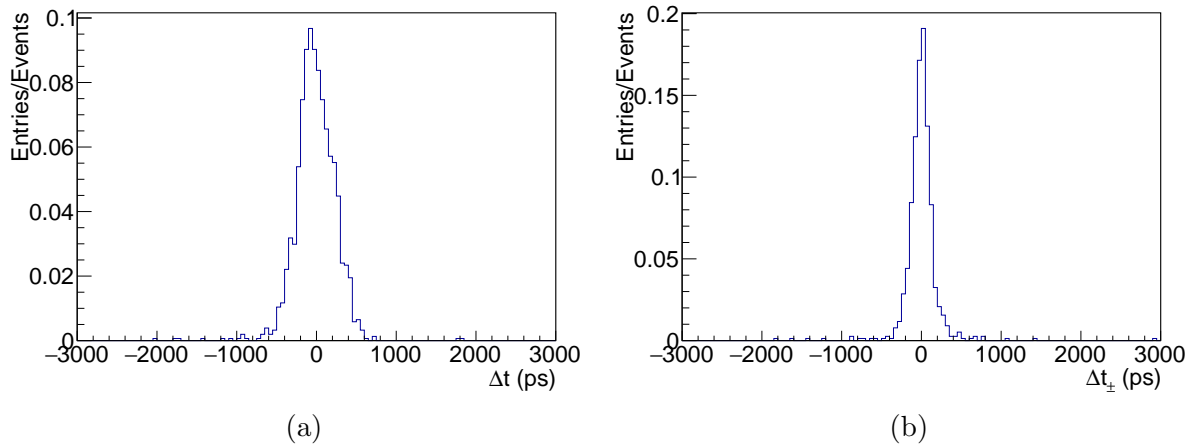
Figure 3.5: Comparison of the histograms of Δt (a) and $\Delta t_\pm$ (b).

Using Δt it will turn out to be not rappresentative of the TOF signal, as we can see in Figure 3.5a.

It is possible to bypass this problem taking advantage of the fact that t_0 is the same for the two particles originated from the J/ψ (the lifetime of the J/ψ is very short so we assume the time from the collision to the decay negligible), so Δt_+ and Δt_- are correlated as we can see in Figure 3.6. We can then introduce the quantity

$$\Delta t_\pm = \Delta t_+ - \Delta t_- = t_+ - t_{exp+} + \cancel{t_0} - (t_- - t_{exp-} + \cancel{t_0}) \tag{3.1}$$

Where the contribution of t_0 cancels out and the variance $\sigma^2_{\Delta t_\pm}$ will become:

$$\sigma^2_{\Delta t_\pm} = 2\sigma^2_t + 2\sigma^2_{t_{exp}} \simeq 2\sigma^2_t \tag{3.2}$$

the uncertanty on t_{exp} is negligible compared to σ_t (~ 2 ps [2]). $\Delta t_\pm$ has then been used throughout the analysis. We can see in Figure 3.5b that the width is considerably reduced using $\Delta t_\pm$.

3.3 q-Gaussian

Earlier in this chapter we introduced the fact that the TOF signal does not seem to follow a pure gaussian distribution and shows a slow decreasing tail as in Figure 3.1. As we will soon see, the newly introduced variable $\Delta t_\pm$ follows a similar trend, finding the

---

[2]When considering particles in relativistic regime, as the muons in the present analysis, we have that misevaluation of the momentum of the particle will have a minimal effect on the evaluation of the velocity. An extimation of $\sigma_{t_{exp}}$ is possible calculating t_{exp}, assuming a resolution on the momentum of 2% [10].
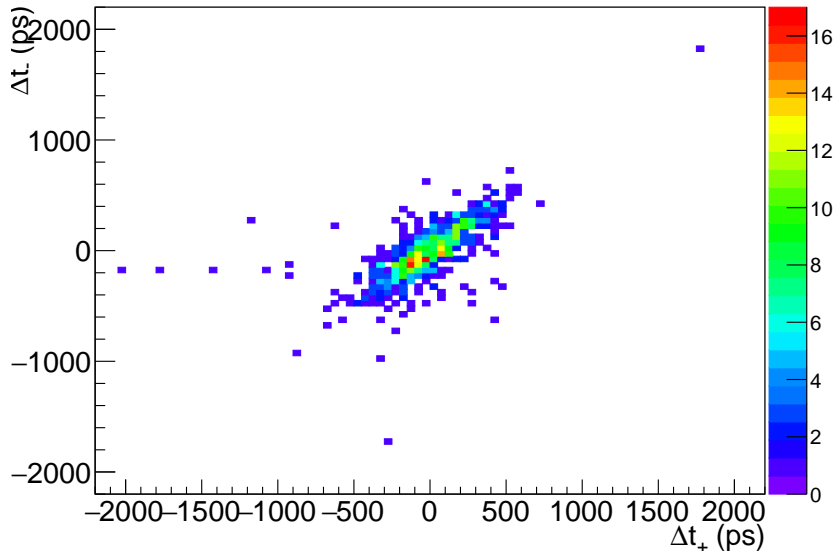
Figure 3.6: Δt of the positive muon versus the negative one.

gaussian not suitable to represent the data due to slow decreasing tail on both side of the peak. To be able to describe the signal we can introduce an alternative model to the Gaussian: the q-Gaussian [11]. This is a generalization of the Gaussian distribution and it is described by the distribution:

$$f(x) = C_{q,\sigma} e_q(-x^2/\sigma),$$

where $C_{q,\sigma}$ is a normalization constant and

$$e_q(x) = [1 + (1-q)x]^{\frac{1}{1-q}}.$$

is the q-exponential. In the limit $q \rightarrow 1$ the q-exponential is the normal exponential. The parameter q caracterizes the shape of the q-Gaussian and the parameter σ is a positive parameter which express the width of the curve. The advantage of introducing this distribution is that adding only one degree-of-freedom allows us, with a simple model, to better fit the signal defined as $\Delta t_{\pm}$ [3]. A comparison of the q-Gaussian and the Gaussian distributions is shown in Figure 3.7a. We can see in Figure 3.7b that, while the Gaussian fails to fit properly the data, the q-Gaussian is accurate. A constant function which rappresents the background noise has also been added to the fitting functions ised in the analysis (blue dashed line).

---

[3]The theoretical implications arising from the use of the q-Gaussian distribution will not be object of this study.
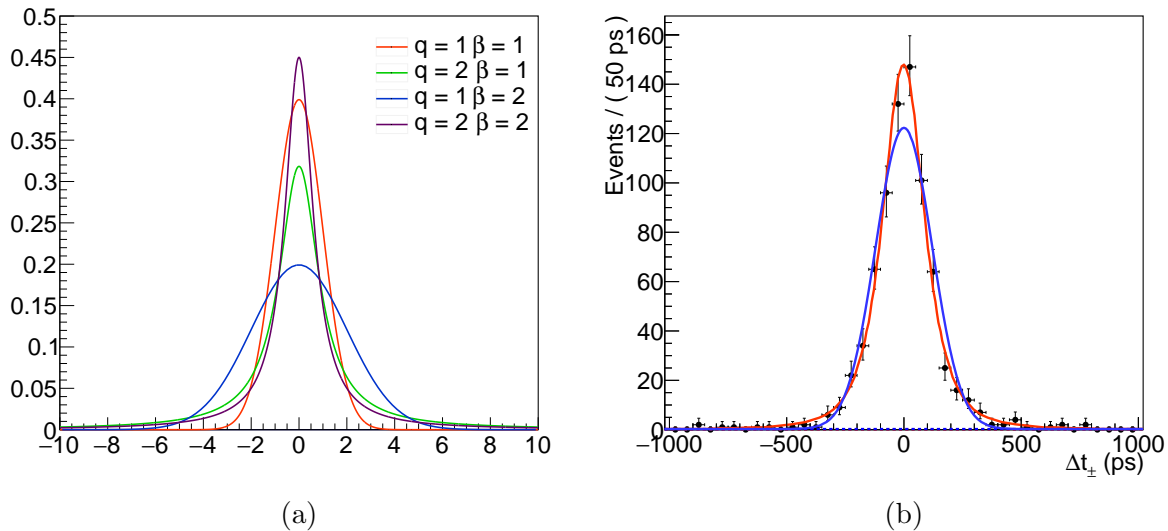
Figure 3.7: Q-Gaussian distribution for some values of q and β (a). The curves with q=1 rappresent Gaussians. Gaussian (blue) and q-Gaussian (orange) fit of the data (b).

3.4 Cut selection

During the analysis some cuts, which *a priori* were thought to affect the purity of the signal, have been tested to verify if there would be a significant effect on $\Delta t_\pm$ when applying the cut. To do so it has been necessary to simultaneously compare the parameters q and σ in the q-Gaussian model. The cuts that have been analized are:

- number of tracks in the TPC,

- number of clusters in the TOF associated with the track,

- J/psi momentum,

- mass cut and study of the tracks outside the mass range selected.

To analize the compatibility, the sample was divided in indipendent sub-samples which have been compared graphing bidimentional contours of the parameters' minimization, highlighting their compatiblity up to two standard deviation. The first two cuts have been taken in consideration trying to reduce the possibility of mismatching between the reconstructed track and the real path of the particle. We can see in Figure 3.8a and Figure 3.8b that in both cases the difference between the sub-samples is not significant so both of the cuts have not been considered necessary.

The other two cuts are related to particle detection as discussed in Section 3.1. We can see in Figure 3.9b how restrictiong to coherent J/ψ (pt<0.1 GeV/c) has no significant
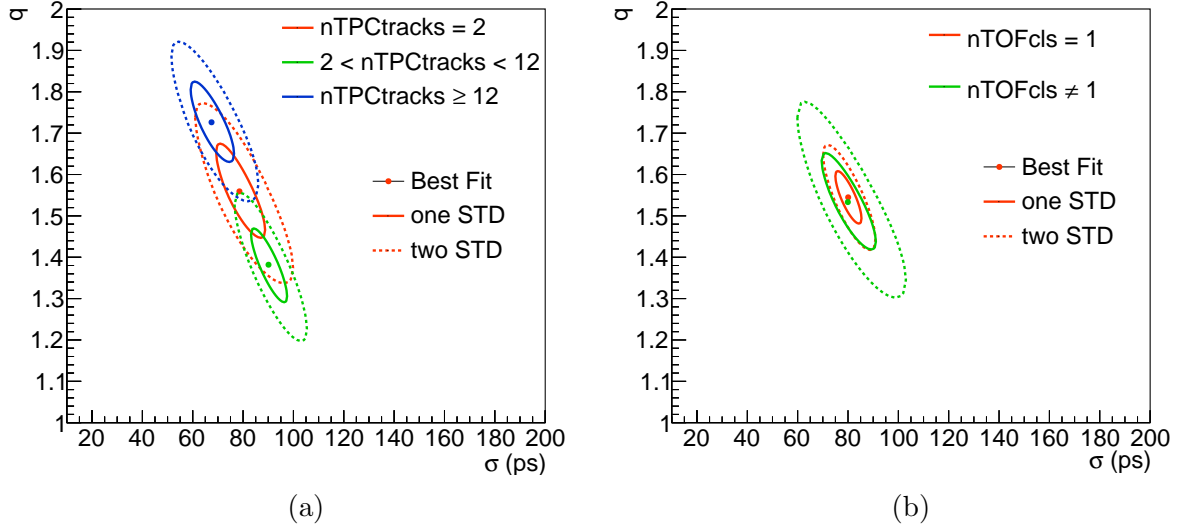
Figure 3.8: Contour graphs of indipendent sub-samples for the number of TPC track (nTPCtracks) cut (a) and the number of cluster in the TOF (nTOFcls)(b). nTOFcls≠1 rapresents events where at least one track has more then one cluster associated in the TOF. In both cases the contours overlap within less then two standard deviations.

impact on the final result. An interesting result can be obtained from Figure 3.9a where we can clearly see how the sub-sample of particles with lower mass then the J/ψ have significantly different behaviour then events with mass in the J/ψ region. Events with mass larger then the J/ψ region do not show a difference with respect to J/ψ events. The cut on the invariant mass has then been mantained.

3.5   Results

In the last section has been possible to decide which cuts have a significant impact on the TOF signal in order to achieve the best cleanliness without excessively compromising the statistic. On the other hand it has to be noted that the number of J/ψ-like events is very limited and the conclusions on the actual impact of the various attempted cuts would benefit from the new LHC data coming in 2018 with a ten times larger Pb-Pb data sample. Figure 3.10 shows the $\Delta t_{\pm}$ distribution resulting from the data, after the application of the cuts. A q-Gaussian fit gives us the caracteristic parameters (q, σ) which are shown in Figure 3.10. The parameters minimization contours are shown in Figure 3.11. Using Equation 3.2 we can obtain the resolution of the TOF detector $\sigma_t = 56.5 \pm 3.3$ ps.

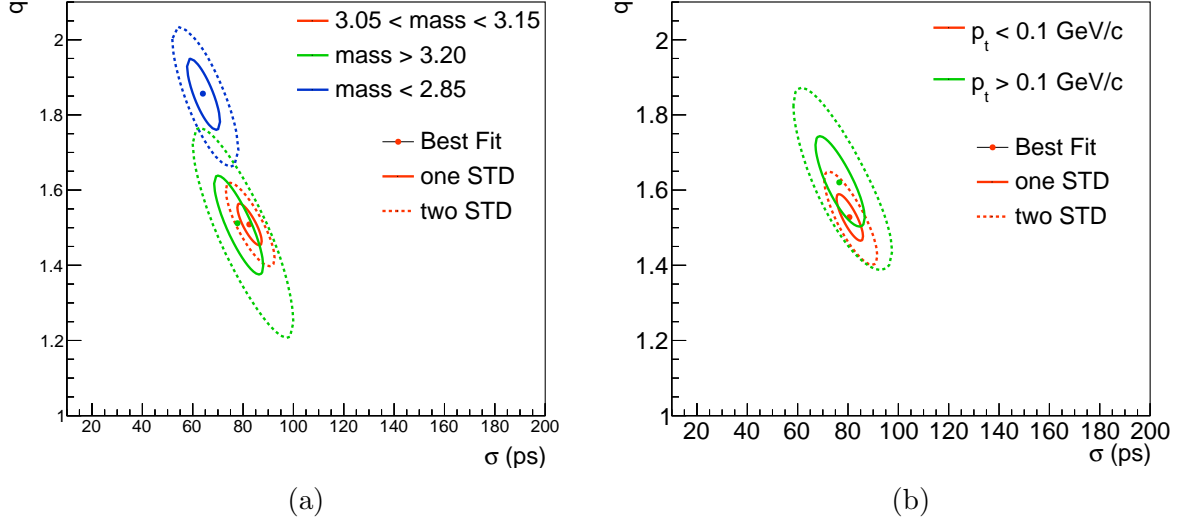As a confirmation of the results obtained a model has been introduced for reppre-

Figure 3.9: Contur graphs of indipendent sub-saples of invariand mass (mass is expressed in GeV) (a) and Pt (b) for selected ranges of the reconstructed particle. The red contours represent coherent J/ψ.

senting the TOF signal. We can define the function $f(x)$ as:

$$f(x) = \begin{cases} q=1 \text{ if } \Delta t < 0 \\ q = q_{TOF} \text{ if } \Delta t > 0 \end{cases} \tag{3.3}$$

composed by a Gaussian for negative values and a q-Gaussian for positive values of Δt. The parameters q and σ can be obtain deconvoluting the signal $\Delta t_\pm$ with the function $f(x)$.

The function $f(x)$, defined by Equation 3.5, can be used in more general contexes as that of high multiplicity pion events. The function $f(x)$ has been applyed to the same data used for the histogram in Figure 3.1, with the parameters obtained with the deconvolution: $q = 1.69 \pm 0.05$ and $\sigma = 57.4 \pm 3.2$ ps. We can observe in Figure 3.12 how the slow decreasing tail is well represented by the model just introduced. These events include a much higher noise component then those used in our analysis. A flat noise function has been added so the data are well represented in the central region of the peak. A more complete study would be necessary to reppresent correctly the tail where the noise component becomes more relevant. This task will not be carried through in this analysis.
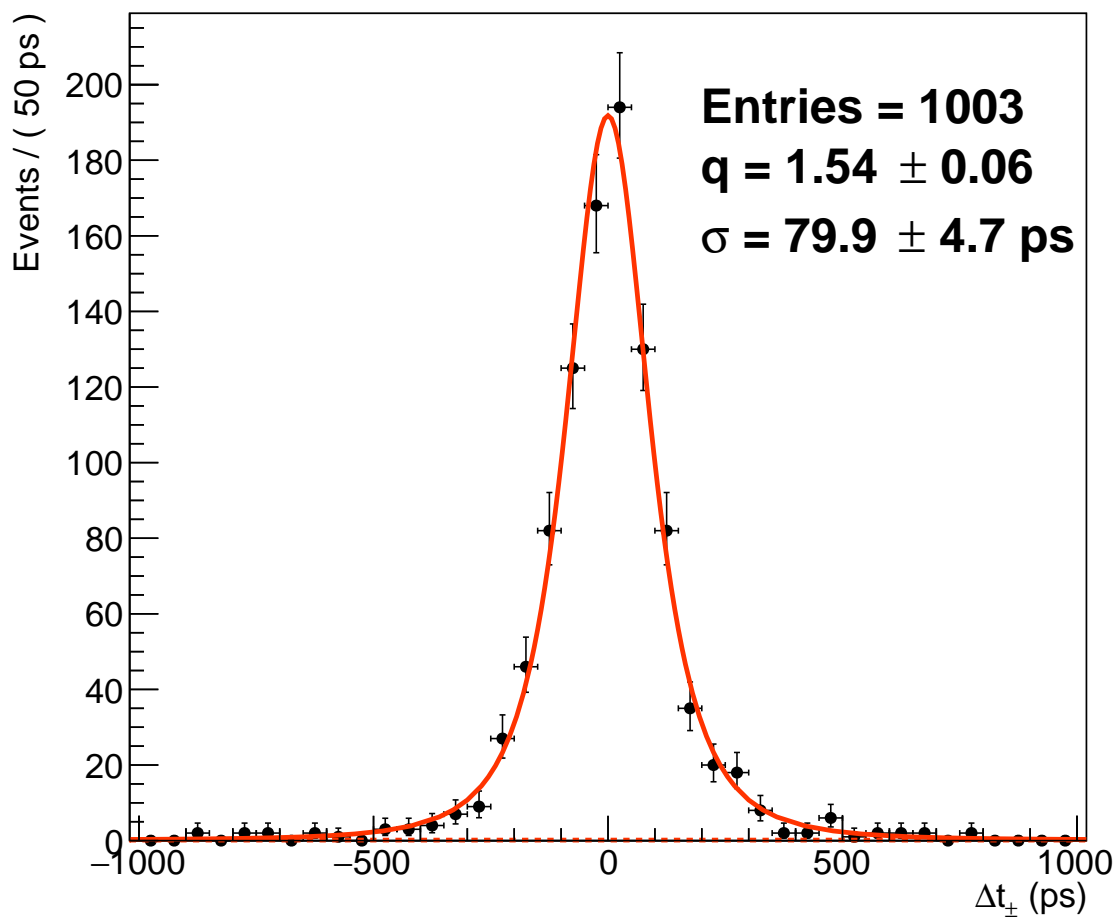
Figure 3.10: $\Delta t_\pm$ of dimuons from J/ψ decays. The solid line indicates the q-Gaussian fit with the parameters σ and q shown. An uniform background noise has been added (dashed line).
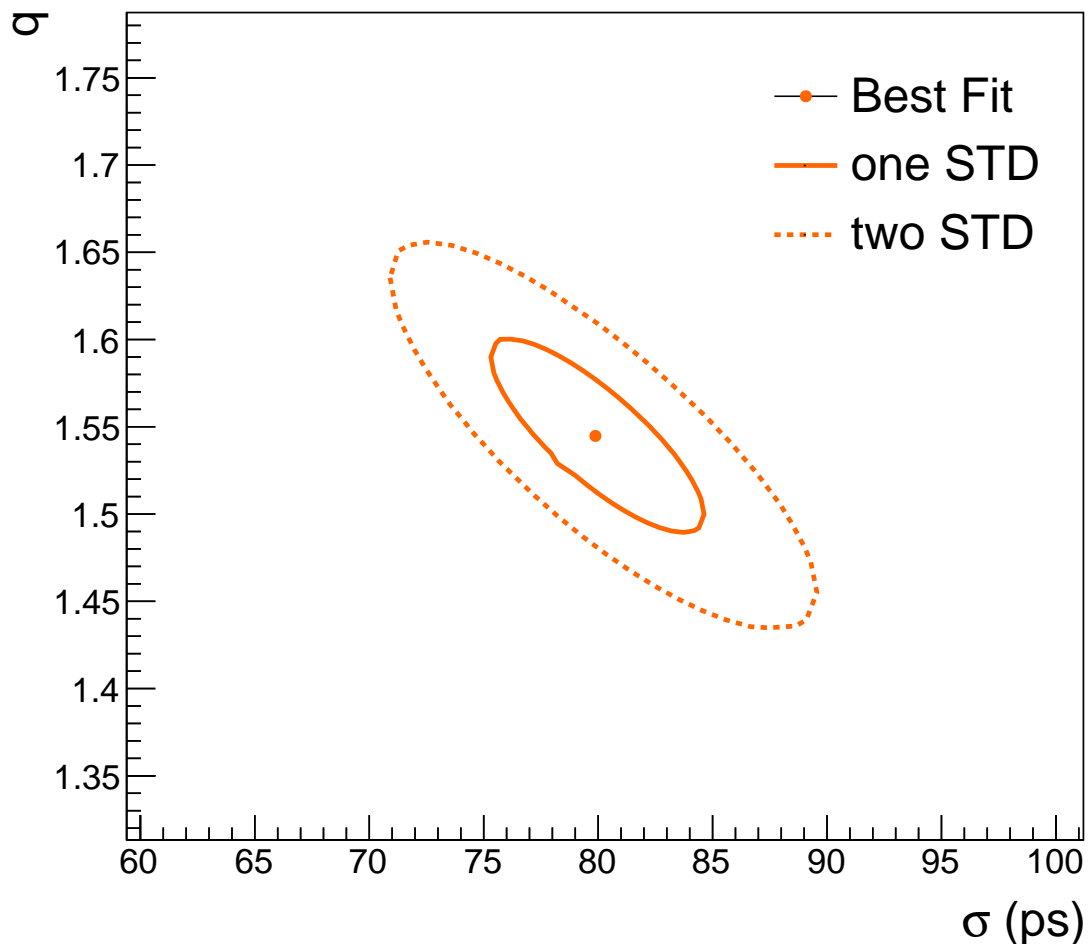
Figure 3.11: Contour graph of the parameters q and σ obtained when fitting the histogram in Figure 3.10.
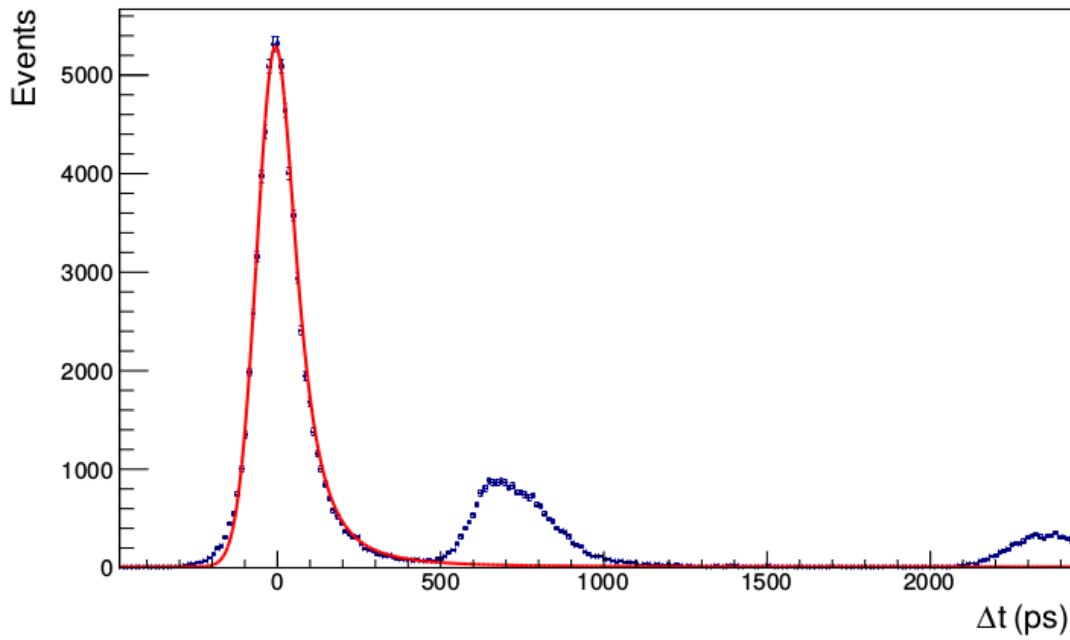
Figure 3.12: Function $f(x)$, defined by Equation 3.5, applied to the same events as those in Figure 3.1.

Chapter 4

Conclusions

In the present analysis a significant improvement have been achieved on the study of the TOF detector signal response. With the introduction of the q-Gaussian and a model which combines it with the Gaussian, the data can be well fitted by using the parameters (q and σ) obtained through the analysis.

It has also to be noticed that the results obtained in Section 3.4 revealed that the impact of cuts which could potentially affect the signal's width was not statistically significative. On the other hand the unusual behaviour of particles outside the J/ψ invariant mass region necessitate further study. Due to the limited number of J/ψ available for the analysis the study can be improved by the significantly larged data sample which will be available in the coming 2018 Pb-Pb run.

Bibliography

[1] S. Bethke. "Experimental tests of asymptotic freedom". In: *Progress in Particle and Nuclear Physics* 58.2 (2007), pp. 351–386. ISSN: 0146-6410. DOI: `https://doi.org/10.1016/j.ppnp.2006.06.001`. URL: `http://www.sciencedirect.com/science/article/pii/S0146641006000615`.

[2] H. C. Chandola, Garima Punetha, and H. Dehnen. "Bag model of hadrons, dual QCD thermodynamics and Quark-Gluon Plasma". In: (2015). arXiv: `1501.01153 [hep-ph]`.

[3] Betty Abelev. "Strangeness with ALICE: from pp to Pb-Pb". In: *Proceedings, PLHC2012: Physics at the LHC 2012 (PLHC2012): Vancouver, BC, Canada, June 4-9, 2012*. 2012. arXiv: `1209.3285 [nucl-ex]`.

[4] T. Matsui and H. Satz. "J/ψ Suppression by Quark-Gluon Plasma Formation". In: *Phys. Lett.* B178 (1986), pp. 416–422. DOI: `10.1016/0370-2693(86)91404-8`.

[5] Jaroslav Adam et al. "Differential studies of inclusive $J\psi$ and $\psi(2S)$ production at forward rapidity in Pb-Pb collisions at $\sqrt{s_{\mathrm{NN}}} = 2.76$ TeV". In: *JHEP* 05 (2016), p. 179. DOI: `10.1007/JHEP05(2016)179`. arXiv: `1506.08804 [nucl-ex]`.

[6] Robert L. Thews, Martin Schroedter, and Johann Rafelski. "Enhanced J/ψ production in deconfined quark matter". In: *Phys. Rev.* C63 (2001), p. 054905. DOI: `10.1103/PhysRevC.63.054905`. arXiv: `hep-ph/0007323 [hep-ph]`.

[7] C. Patrignani et al. "Review of Particle Physics". In: *Chin. Phys.* C40.10 (2016), p. 100001. DOI: `10.1088/1674-1137/40/10/100001`.

[8] Elaine Abbas et al. "Charmonium and e + e - pair photoproduction at mid-rapidity in ultra-peripheral Pb-Pb collisions at $\sqrt{s_{\mathrm{NN}}} = 2.76$ TeV". In: 73 (Nov. 2013), pp. 1–18.

[9] Nicola Rubini. "Analysis of the TOF resolution: a "tomography" study of the time of flight detector of the ALICE experiment at the LHC". PhD thesis. URL: `http://amslaurea.unibo.it/14100/`.

[10] Pierre Vande Vyvre. "Performance of the ALICE Experiment at the CERN LHC". In: (Feb. 2014).

[11]   Constantino Tsallis. "Nonadditive entropy and nonextensive statistical mechanics - An overview after 20 years". In: 39 (Aug. 2009), pp. 337–356.